In Situ ETEM Study of Composition Redistribution in Pt-Ni Octahedral Catalysts for Electrochemical Reduction of Oxygen

Yung-Tin Pan, Jianbo Wu, Xi Yin, and Hong Yang
Dept. of Chemical and Biomolecular Engineering, University of Illinois at Urbana-Champaign, 206 Roger Adams Laboratory, MC-712, 600 South Mathews Avenue, Urbana, IL 61801

DOI 10.1002/aic.15070
Published online October 15, 2015 in Wiley Online Library (wileyonlinelibrary.com)

Dynamics of thermally induced composition redistribution of sandwich-like Pt-Ni octahedral electrocatalysts was studied in situ using a variable-temperature environmental transmission electron microscope (ETEM). Dislocations were observed and on heating treatment moved toward the surface over time, resulting in an alloy nanoparticle with significant increase Ni content on the surface, which was confirmed by X-ray photoelectron spectroscopy. The thermally treated Pt-Ni octahedral catalysts showed significant improvement in catalyzing oxygen reduction reaction over the as-made nanoparticles, reaching values of 1.4 A/mg$_{Pt}$ in mass activity and 4.8 mA/cm$^2_{Pt}$ in area specific activity. Our study shows the important effect of postsynthesis treatment on the optimization of Pt and Ni atomic distribution, thus the catalytic activity and stability; and the power of in situ ETEM in understanding the structural origin of enhanced catalytic performance with atomic level of details. © 2015 American Institute of Chemical Engineers *AIChE J*, 62: 399–407, 2016

Keywords: Pt-Ni, core-shell, electrocatalysis, oxygen reduction reaction, environmental transmission electron microscope

Introduction

Electrocatalysts are important for a range of applications, such as polymer electrolyte membrane fuel cell,[1] battery,[2,3] and solar-fuel device.[4] Heterogeneous electrocatalysis usually involves the adsorption of reactant (molecule or ion), electron transfer, and desorption of product from the surface. Thus, surface state is key in electrocatalytic reaction, and the ability to manipulate composition and atomic structure on or near the catalyst surface can have great impact on the performance in both activity and stability. In this context, bimetallic catalyst becomes increasingly important for electrochemical reaction because the process can be extremely sensitive to surface structure and composition.[1,5–7] For the control of catalysts with well-defined surfaces, solution phase synthesis is proved to be a promising route, because this method is capable for producing monodisperse nanoparticles with uniform shape and overall composition.[8,9] These structural parameters are not always independently tunable although,[8,10] because several factors determine the final surface composition, which can be related to global surface energy and phase behavior (alloy or intermetallic).[9,11]

Surface composition and structure of a pristine bimetallic nanoparticle are unusually determined by the element that has the lower intrinsic surface energy. However, when the particle is exposed to a reactive environment or in the presence of capping ligand in solution, the dominant surface species becomes the one that has a lower overall energy, which is a combination of intrinsic surface energy and adsorption energy of molecules on specific atomic sites.[12,13] It has been demonstrated the surface composition of bimetallic nanoparticle can be very sensitive to reactive environments using *in situ* X-ray spectroscopy-based techniques.[12–18] Moreover, the surface composition responds dynamically to the environment, showing reversibility under cyclic gas atmospheres.[12] In addition to X-ray-based techniques, using the latest environmental transmission electron microscope (ETEM),[19–22] one can expect to obtain valuable information on the structural or morphological changes of nanoparticles *in situ* at high-spatial resolution under reactive atmospheres.[23] A combination of both X-ray and ETEM techniques can, therefore, provide a comprehensive picture of the dynamic behavior of bimetallic nanoparticles to develop optimal processing conditions and design principles.

Herein, we present the structural changes of as-made Pt-Ni octahedral catalysts *in situ* during the postsynthesis thermal treatment under processing temperatures using ETEM. The corresponding as-made and thermally treated carbon-supported Pt-Ni octahedral catalysts were studied for the reduction of oxygen under acidic conditions. So far, a large number of Pt-based alloy nanoparticles were shown to be excellent oxygen reduction reaction (ORR) catalysts.[1,7,8,10,24–29] Transition metal segregated in the subsurface is a critical feature of these ORR catalysts of Pt-M (M=transition metal) nanoparticles.[30–33] The optimization in structure has often been done via postsynthesis treatment thermally or electrochemically.[34,35] Among the alloys

Additional Supporting Information may be found in the online version of this article.

Yung-Tin Pan and Jianbo Wu contributed equally.

Correspondence concerning this article should be addressed to H. Yang at hy66@illinois.edu.

of Pt and transition metals, Pt_3Ni was shown to be among the optimal alloy compositions that have the highest ORR performance. The as-made octahedral Pt_3Ni catalyst tends to have high Ni content preferentially segregated on surface of {111} facets.[32] On treatment in chemical or electrochemical environments, these Ni atoms leached out preferentially from the {111} facets, and the catalyst particles evolved into various etched structures, such as, concave octahedron, hexapod, or nanoframe.[36–38]

We choose carbon-supported, sandwich-type Pt-Ni octahedral nanoparticles in this work. The *in situ* ETEM study was performed at a mild annealing temperature of 200–210°C under vacuum. This condition was also used to post-treat as-made Pt-Ni octahedral nanoparticle catalysts on carbon support. *Ex situ* X-ray photoelectron spectroscopy (XPS) was used to study both the as-made and annealed (210°C, vacuum) Pt-Ni nanoparticle catalysts; while cyclic voltammetry (CV) and polarization curve were used to examine their ORR performance.

Experimental

Materials and chemicals

All chemicals were used as received without further purification. Platinum acetylacetonate ($Pt(acac)_2$, Strem Chemical, 98%); nickel acetylacetonate ($Ni(acac)_2$, Sigma-Aldrich, 95%); oleylamine (OAm, Sigma-Aldrich, technical grade, 70%); oleic acid (OAc, Sigma-Aldrich, technical grade, 90%); diphenyl ether (Sigma-Aldrich, 99%); n-butylamine (Sigma-Aldrich, 99.5%); hexane (Sigma-Aldrich, >95%); chloroform (Macron, >99%); ethanol (Decon Labs, 200 proof); methanol (Macron, >99%); argon gas (Ar, Airgas, C.P. grade); carbon monoxide gas (CO, Airgas, C.P. grade).

Synthesis of Pt-Ni octahedral nanoparticles

To synthesize Pt-Ni octahedral nanoparticles, a solution of 20 mg (0.05 mmol) of $Pt(acac)_2$, 7 mg (0.027 mmol) of $Ni(acac)_2$ was mixed with 9 mL of oleylamine (OAm), 1 mL of diphenyl ether, and 50 μL of oleic acid (OA) in a 25-mL three-neck round bottom flask immersed in an oil bath at 130°C. The flask was connected to a Schlenk line through a condenser. The reaction mixture turned into a transparent yellowish solution at this temperature after 2 min. The flask was then evacuated with a rotary pump (Edward RV 12) and purged with Ar for six cycles to remove air and moisture. The solution was then bubbled with CO gas and transferred to a second oil bath at 210°C. Throughout the process, the flask was connected to the Schlenk line. The typical flow rate of CO gas was set at 120 cm^3/min and the reaction time was 30 min. The rest of steps followed the procedure for synthesis of Pt-Ni octahedral nanoparticles reported previously.[8] The solid products were washed and separated by dispersing the reaction mixture in 2 mL of chloroform and 10 mL of ethanol, followed by centrifugation at 5000 rpm for 5 min. This procedure was repeated three times. The final products were dispersed in hexane for further characterization.

Preparation of carbon-supported catalysts

Carbon black (Vulcan XC-72) was used as support for making platinum nickel catalysts (Pt-Ni/C). In a standard preparation, carbon black particles were dispersed in chloroform and sonicated for 1 h. A designed amount of Pt-Ni nanoparticles suspension in hexane was added to this dispersion of carbon black at the nanoparticle-to-carbon-black mass ratio of 20:80. This mixture was further sonicated for 30 min and stirred overnight. The resultant solids were precipitated out by centrifugation and dried under an argon stream. The solid product was then redispersed in n-butylamine at a concentration of 0.5 mg-catalyst/mL in a capped glass vial. The mixture was kept under stirring for 3 days under ambient air conditions and then collected using a centrifuge at a rate of 5000 rpm for 5 min. The precipitate was redispersed in 10-mL methanol by sonicating for 15 min and then separated by centrifugation. This procedure was repeated three times. The final samples were dispersed in ethanol for further characterization. For *ex situ* thermal treatment, carbon-supported catalysts were annealed at 210°C in a tube furnace (GSL-1500X, MTI Corporation) for 1 h and cooled down under vacuum (9.8 kPa or 0.097 atm). The treated catalyst was then used for electrochemical measurements.

Characterizations

Transmission electron microscopy (TEM) and high-resolution transmission electron microscopy (HR-TEM) micrographs were taken on a FEI TECNAI F-20 field emission microscope at an accelerating voltage of 200 kV. Scanning transmission electron microscopy (STEM) micrographs and energy dispersive X-ray (EDX) elemental spot analysis and line scans were performed using the high-angle annular dark-field mode on JEOL 2010F STEM with Schottky field emitter at an accelerating voltage of 200 kV. Inductively coupled plasma optical emission spectrometry (ICP-OES) was performed using a Perkin Elmer 2000DV ICP-OES spectrometer. XPS was acquired using Kratos Axis ULTRA (Manchester UK) spectrometer with a monochromatic Al source. The XPS spectrum analysis was done using CasaXPS software with Shirley type baseline. To make an XPS specimen, as-made Pt-Ni octahedral nanoparticles, after extensive washing with chloroform, were drop-casted on Si wafer and treated under the same condition as mentioned above. The atomic ratio between Pt and Ni were calculated by integrating Pt 4f (60–84 eV) and Ni 2p (845–885 eV) peaks with a sensitivity factor of 6.115 and 3.845, respectively.

In situ ETEM study

In situ heating experiment was conducted using a Hitachi H9500 ETEM at an accelerating voltage of 200 kV. This ETEM is equipped with a variable-temperature heating holder made of a tungsten wire. Carbon-supported catalyst dispersed in ethanol was loaded on the tungsten heating wire, which was premounted on the *in situ* holder, using a fine-tip paint brush. The catalyst was transferred by dipping the brush in the ethanol solution and deposited on the heating wire by gentle brushing. The catalyst-deposited heating wire was then left sitting on bench for 30 min to allow the evaporation of ethanol. The holder was then introduced into the Hitachi H9500 ETEM and connected to a DC power supply for resistive heating.

Survey of the sample was done at room temperature under standard operating conditions. Once the particle of interest was located, electron beam was blocked by closing the gun valve and temperature of heating wire was raised. Temperature of the sample was determined by the current-temperature relation chart (Hitachi). The current was slowly increased to 390 mA (200°C) and maintained throughout the rest of the experiment. Once the current reached 390 mA, TEM micrographs were recorded using the Gatan Orius SC200 CCD

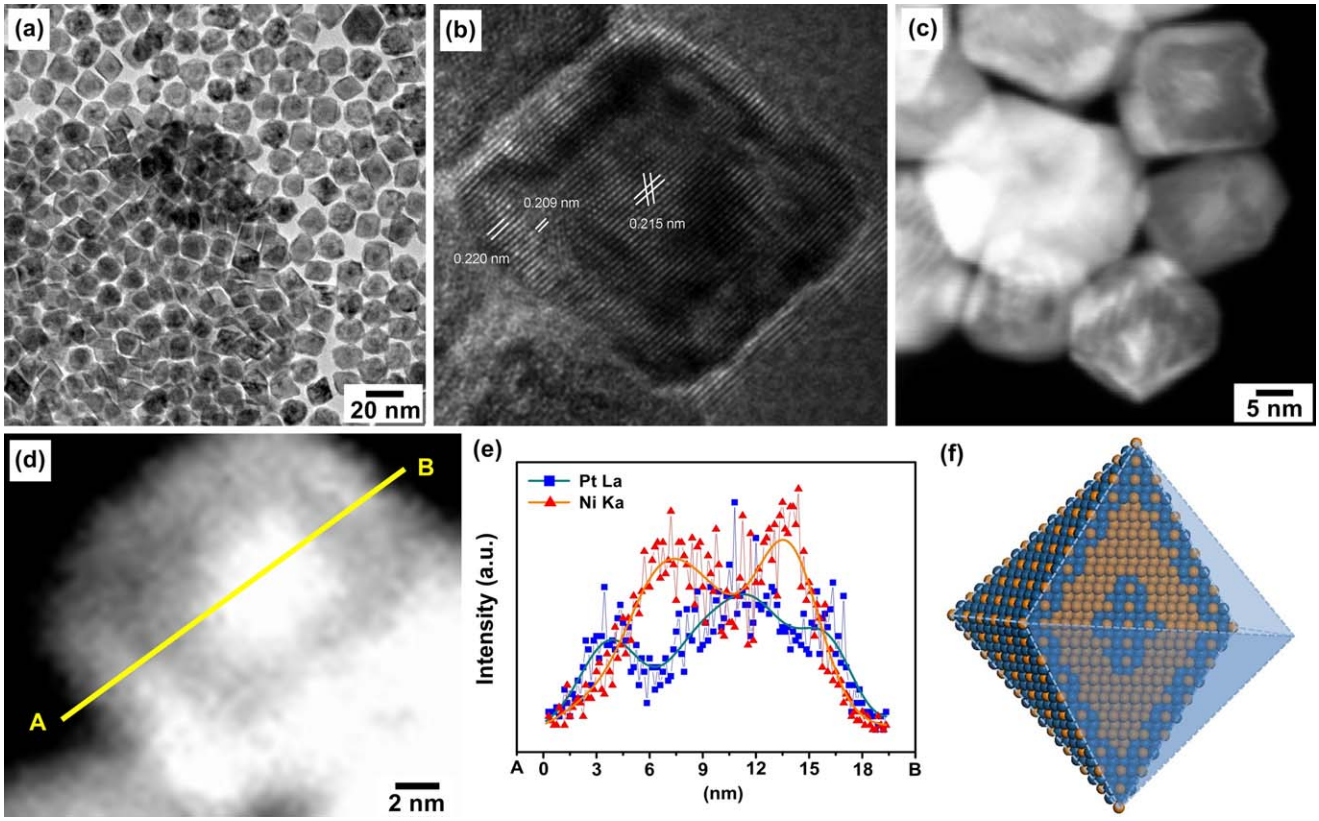

Figure 1. EM characterization of as-made Pt-Ni octahedral nanocrystals: (a) low and (b) high magnification TEM micrographs, (c) low and (d) high magnification dark-field STEM images, (e) EDX line scans for Pt and Ni elements (square: Pt, triangle: Ni) and (f) schematic drawing of the sandwich-like three-layered structures.

[Color figure can be viewed in the online issue, which is available at wileyonlinelibrary.com.]

camera, and Gatan digital micrograph software. The TEM images were recorded by taking screen shot videos with CamStudio software during the course of experiment. Electron irradiation was kept minimized during the course of experiment and the gun valve was opened only during image acquisition, which was typically less than 1 min with a current density of 1.18×10^{-11} A/cm^2. The sample was then left in dark for another 5 min before the next imaging cycle. Image analysis and processing was done using Digital Micrograph (DM, Gatan) and ImageJ software. Detail procedures for image processing are described in Supporting Information.

Electrochemical measurement

A three-electrode cell was used to measure the electrochemical properties of these alloy catalysts. The working electrode was a glassy-carbon rotating disk electrode (RDE) (area: 0.196 cm^2). A 1 cm^2 platinum foil was used as the counter electrode and a HydroFlex hydrogen electrode was used as the reference, which was placed in a separate compartment. Hydrogen evolution reaction was used to calibrate this hydrogen electrode before the tests. All potentials were referenced to the reversible hydrogen electrode (RHE). The electrolyte was 0.1-M $HClO_4$ aqueous solution, diluted from 70% double-distilled perchloric acid (GFS Chemicals) with MilliporeQ ultrapure water. The mass of metal in each Pt-Ni/C catalyst was determined by thermogravimetric analysis (TGA) using an SDT-Q600 TGA/DSC system from TA Instruments at a ramp rate of 10°C/min to 600°C in air followed by annealing at 600°C for 30 min under a forming gas of 5% hydrogen in argon at a flow rate of 50 mL/min. To prepare the working electrode, 5 mg of the Pt-Ni/C catalyst (20% based on the weight of alloy nanoparticles) was dispersed in 10 mL of the mixed solvent and sonicated for 5 min. The solvent contained a mixture of deionized water, isopropanol, and 5% Nafion at the volumetric ratio of 8:2:0.05. Twenty microliter of the suspension was added onto the RDE by a pipette and dried in air. The loading amount of Pt-Ni alloy nanocatalysts on the RDE was determined to be 9.3 μgPt/cm^2. The CV measurement was carried in argon-saturated 0.1-M $HClO_4$ solution at room temperature with a scan rate of 50 mV/s. ORR activity was determined in a 0.1-M $HClO_4$ solution which was purged with oxygen for 30 min prior to, and during testing. The scan rate for ORR measurement was set at 10 mV/s in the positive direction. Data were used without iR-drop correction.

Results and Discussion

Figure 1 shows the electron microscopy (EM) micrographs, EDX line scan, and a three-dimensional illustration of as-made Pt_3-Ni octahedral catalysts. These nanoparticles showed monodispersity and were uniform in size and shape (Figure 1a). The average edge length of these octahedral nanoparticles was 11.3 ± 1.3 nm. The vast majority of the particles had a dark contrast core and shell with a light contrast layer sandwiched in between. High-resolution TEM (HRTEM) images showed the lattice fringes had a *d*-spacing of 2.15 Å in the core, 2.20 Å in the shell, and 2.09 Å in the layer sandwiched in between (Figure 1b). High-angular dark-field STEM was used to further analyze this unique three-layered structure, because Z contrast is quite distinctive for these two metal

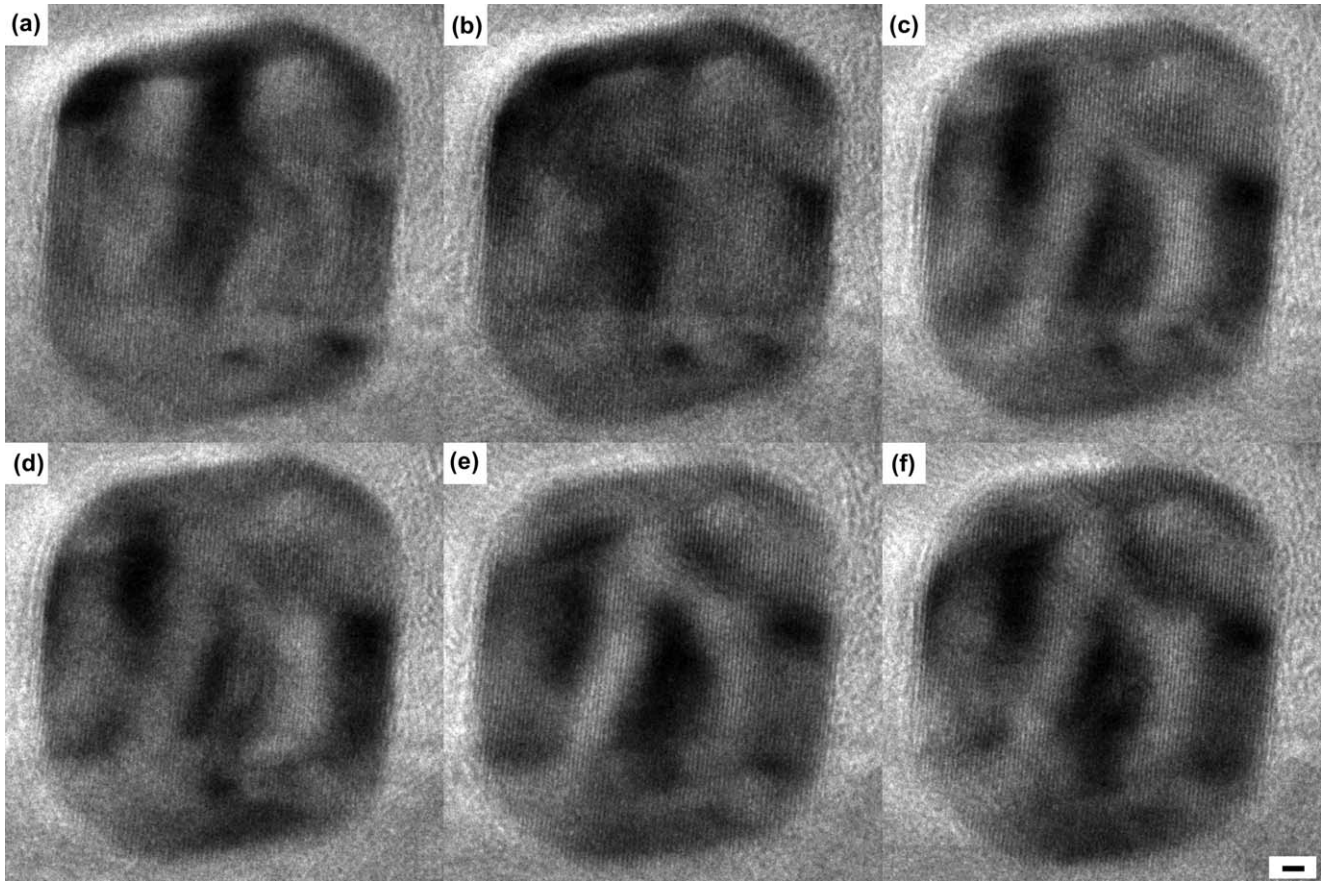

Figure 2. *In situ* TEM micrographs of a Pt-Ni nanoparticle taken under vacuum annealing conditions at 200°C, over a time period of (a) 0, (b) 4, (c) 10, (d) 15, (e) 20, and (f) 25 min, respectively.

Scale bar is 2 nm, applicable to all.

elements in such STEM micrographs (Figures1c, d). The STEM study shows unambiguously the core and shell had higher intensity (heavier metal, i.e., Pt) than the middle layer. Average size of the core was about 5 nm and thickness of the outer surface layer was 1.5 nm, approximately equivalent to seven atomic layers. Thickness of the middle region was ~5 nm.

The EDX line scan (Figure 1e) provides a semiquantitative compositional analysis along the trajectory in Figure 1d. The Pt Lα line had three peaks located in the outer shell and core regions (blue squares fitted with green line), while Ni Kα line had two peaks (orange triangles fitted with red curve) in the subshell layer. A quantitative spot analysis shows that the composition of as-made Pt-Ni octahedral nanoparticle was $Pt_{77}Ni_{23}$ in the central region, $Pt_{54}Ni_{46}$ in the subshell-layer, and $Pt_{71}Ni_{29}$ in the outer shell region (Supporting Information Figure S1). The ICP-OES analysis showed that the nanoparticles have a Pt to Ni atomic ratio of 54:46. These convergence evidence indicates Pt and Ni did not distribute uniformly in as-made octahedral particles, instead they had a sandwiched nanostructure with Pt rich in both the core and shell regions, as being illustrated in Figure 1f.

Figure 2 shows a series of *in situ* HRTEM micrographs of a representative Pt-Ni octahedral nanoparticle taken at 200°C for a time period of 25 min. These micrographs were taken with 5-min intervals with an exposure time of 15–30 s to electron beam during each image acquisition. The contrast inside these TEM nanoparticles varied, reflecting the change in composition and structure, especially those features related to lattice strain. On annealing, boundaries of the 2-nm thick outer

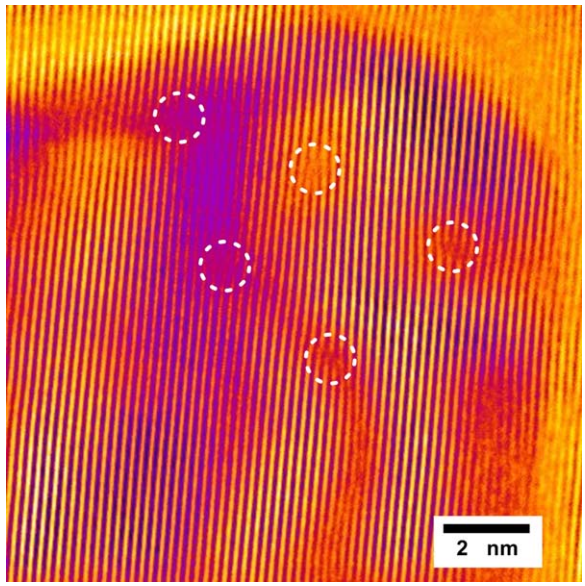

Figure 3. Representative filtered amplitude image of the corner region of a Pt-Ni octahedral nanoparticle.

This image was generated using the top right portion of the image shown in Figure 2a. Position of the dislocations are marked with circles. [Color figure can be viewed in the online issue, which is available at wileyonlinelibrary.com.]

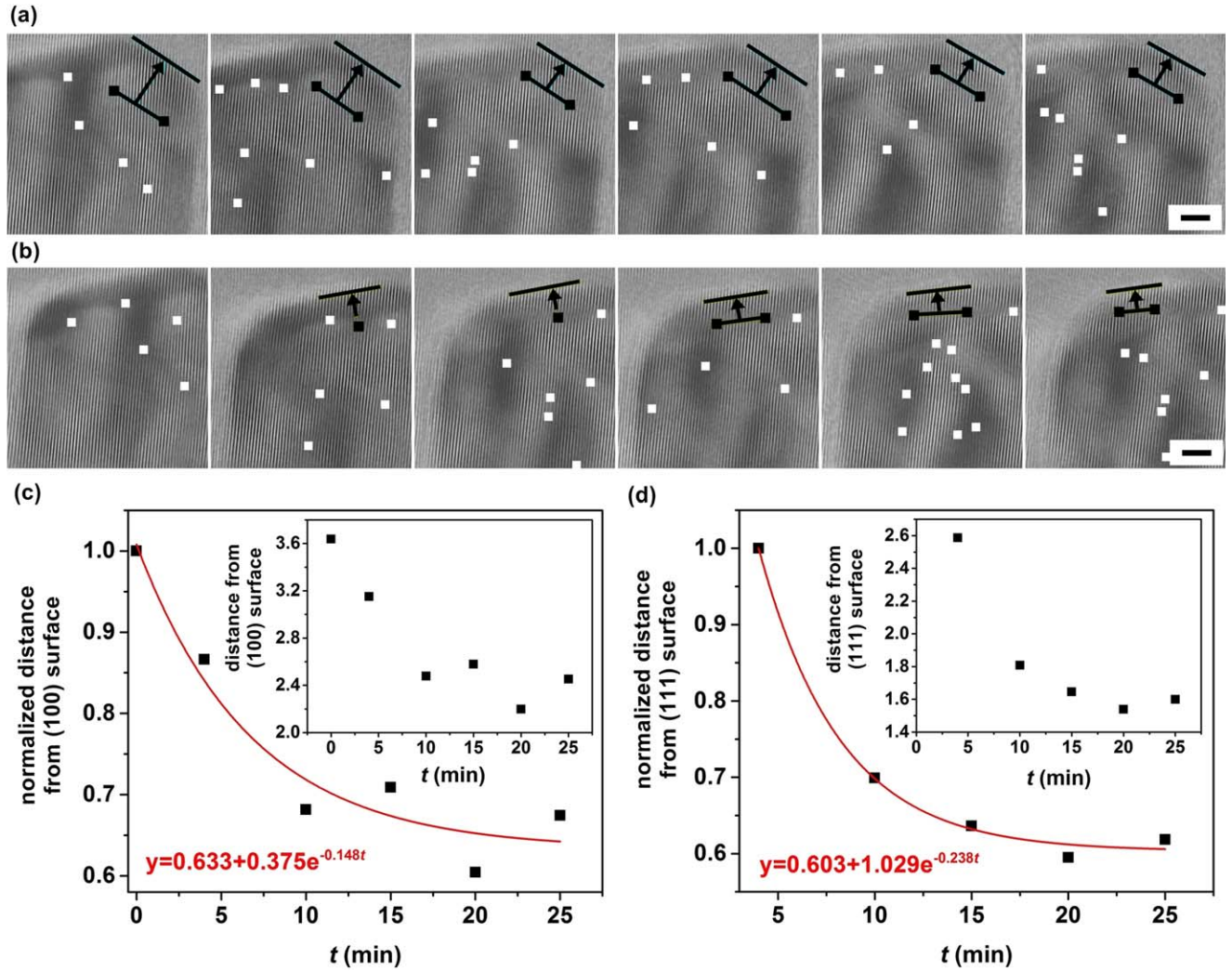

Figure 4. (a, b) TEM micrographs and (c, d) fitting curve of dislocation movement as a function of time along (a, c) <100> and (b, d) <111> directions, respectively, within a Pt-Ni nanoparticle.

The fitting curves were drawn based on the Fick's law. The squares highlight the positions of the edge of dislocation planes. The black squares were used to obtain the distances from the surface. Scale bar is 2 nm, applicable to all. [Color figure can be viewed in the online issue, which is available at wileyonlinelibrary.com.]

shell became less distinguishable over time, accompanied with rounding off of the facets of octahedral nanoparticles. The heterogeneity in composition created strong driving force for atoms to move within the as-made Pt-Ni octahedral nanoparticles at elevated temperatures, resulting in redistribution of both Pt and Ni elements. To extract the lattice movement information from these TEM images, we used the inverse Fourier transform technique to generate filtered images based on diffraction patterns obtained using FFT (see Supporting Information for detail, Figures S2 and S3). The filtered image provides information of the lattice fringes in the <111> direction. Figure 3 is a representative filtered amplitude image of upper right region of the octahedral nanoparticle shown in Figure 2a. The positions of dislocation, highlighted with dashed white circles, were clearly visible in multiple places. As the values of intrinsic (111) lattice spacing between Pt and Ni are quite different (2.265 vs. 2.034 Å), these dislocations likely originated from the misfit and near the boundary regions between Pt-rich core/shell and the subshell layer in between.

Figure 4 shows the TEM micrographs and the fitting curves of the dislocation movement for the above octahedral nanoparticle. The locations of observed dislocations were highlighted with white squares. These dislocations moved outwards and eventually settled near the surface during the course of experiment (Figures 4a, b). As dislocation tends to exist at the position where large lattice mismatch occurs, that is, the dislocations tend to concentrate at the boundaries between the shell and subshell or the subshell and core regions, the migration of dislocations suggest the movement of Ni in the subshell layer toward the surface, or effective counter diffusion of Pt and Ni atoms in the particle. Migration of dislocations toward the surface occurred along both <111> and <100> directions (Figure 4). The dislocation moved about 1.2 nm toward the {100} surface over a period of 25 min (Figure 4c) and 0.78 nm in 20 min toward the {111} surface (Figure 4d). The final positions of the dislocations were about 2.4 nm from the {100} surface and ~1.6 nm from the {111} surface. Distance between the position of dislocation and surface had an exponential decay relationship with respect to time along both directions (Figures 4c, d). Our data also show migration along the <111> direction reaching final stage, that is, steady state, faster than the <100> direction. Fick's second law of one-

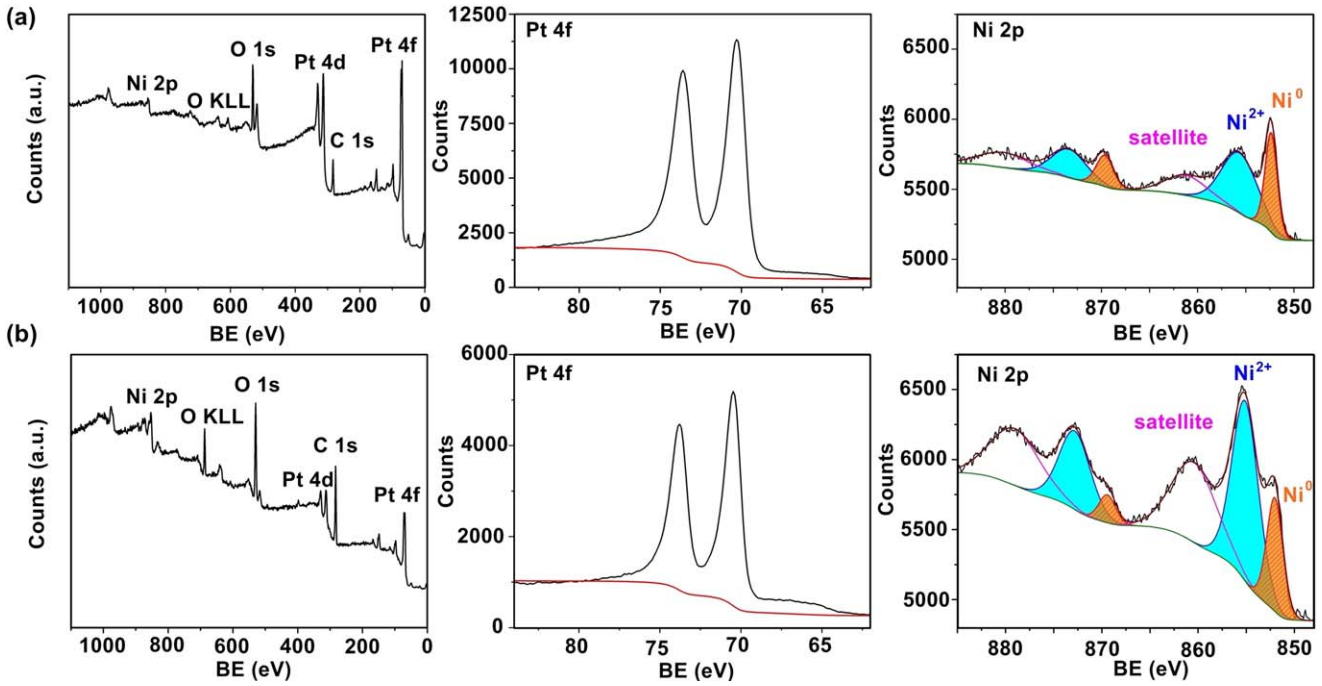

Figure 5. XPS spectroscopy of (a) as-made and (b) vacuum-annealed Pt-Ni octahedral catalysts, showing the survey scan (left), Pt 4f (middle), and Ni 2p (right) regions, respectively.

[Color figure can be viewed in the online issue, which is available at wileyonlinelibrary.com.]

dimensional diffusion was used to gain semiquantitative understanding of the dislocation movement

$$\frac{\partial C}{\partial t} = D\frac{\partial^2 C}{\partial x^2} \tag{1}$$

where C is a function describing the concentration of either Pt or Ni as a function of time (t) and position (x). D is the diffusion coefficient. The solution of the time-dependent term has the general formula of

$$C(x,t) = A(x)\cdot T(t) \tag{2}$$

$$T(t) = e^{-Dk^2 t} \tag{3}$$

where the constant k is inversely proportional to the distance between the two boundaries. Equation 3 is essentially describing how fast the metal atoms reach equilibrium. On reaching equilibrium, the dislocation seized to move toward the surface. Thus, there should be a correlation between the movement of position of dislocation and the migration of metal atoms. If one of the two boundaries is set at the surface and the other is in close proximity to the dislocations, the initial location of the dislocations was 2.59 nm (L_{111}) and 3.64 nm (L_{100}) away from {111} and {100} surfaces, respectively. The ratio between the square of L_{100} and L_{111} (L_{100}^2/L_{111}^2) is 1.975. From Figures 4c, d, the fitted rate constant for dislocations migrating along the (111) Dk_{111} and (100) Dk_{100} directions are 0.238 and 0.148 min^{-1}, respectively, with a ratio of 1.608 between the two. If the diffusivity inside a crystal is independent of the diffusion direction, the ratio should be identical between the fitted rate constant Dk_{100}/Dk_{111} and L_{111}^2/L_{100}^2. The calculation shows a nearly 20% variation between the two values using highly simplified model, indicating that the diffusion coefficient of the dislocation along the <111> and <100> directions might be different, with the diffusion coefficient is about 1.23 times larger in the <100> direction. This phenomena may origin from the different packing density of atoms in the (100) and (111) surfaces, with a less densely packed planes along the <100> direction. The calculated values of diffusion coefficient are on the order of 10^{-2} to 10^{-1} nm^2/min (10^{-22} to 10^{-21} m^2/s) along the <100> and <111> directions. While these values are very rough estimations as the assumption of the fixed boundary conditions could not really be applicable directly in the solid catalyst, they are much higher than the volume diffusion coefficient of Pt and Ni extrapolated from high-temperature measurements (8.63×10^{-8} nm^2/min, or 1.44×10^{-27} m^2/s).[39–41] Hence, the movement of the dislocation should reflect the grain boundary like diffusion assisted by the local atomic movement around the end regions of dislocation planes.[42] A control experiment was performed on the Pt-Ni octahedral nanoparticle at room temperature under similar operation procedure to evaluate the effects of electron beam (Supporting Information Figures S4 and S5). We did not observe the outward movement of dislocations, although we did observe variations is dislocation position.

XPS spectroscopy was performed on the carbon-supported Pt-Ni octahedral nanoparticles before and after annealing in vacuum at 210°C for 1 h (Figure 5). The survey scans indicate the surface contains Pt, Ni and C, and O elements. Pt existed as pure metallic form, judging by the position and shape of the binding energy peaks for Pt 4f lines. Surface Ni was present in both metal and oxide forms, with oxide as the dominant phase, judging by the position of Ni 2p lines. Thus, the binding energy peak at 531 eV, which corresponds to O 1s line, could come from both the surface absorb species and nickel oxides. The observation of surface nickel oxides was expected, as the samples were not stored under inert atmosphere and Ni metal atoms reacted readily with oxygen to form NiO_x on exposure to air. Our XPS data show the surface, including the near surface region, was composed of 90 atomic percent (at %) of Pt

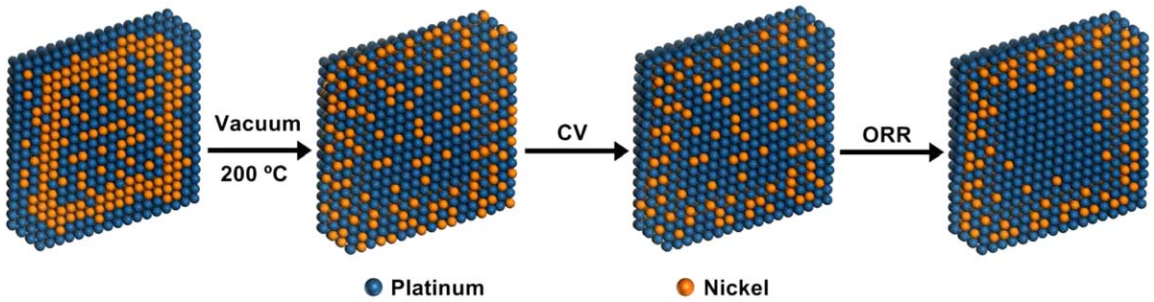

Scheme 1. Proposed change in composition of the sandwich-structured octahedral Pt-Ni ORR catalyst after post-synthesis thermal and electrochemical treatment steps.

[Color figure can be viewed in the online issue, which is available at wileyonlinelibrary.com.]

and 10 at % of Ni for the as-made Pt-Ni octahedral catalyst. The composition changed to 51 at % of Pt and 49 at % of Ni for the surface regions after the sample was treated at 210°C under vacuum for 1 h. The increase of surface Ni content was accompanied with the increase of oxide form of Ni species. Similar relation between surface Ni ratio and its oxidation state was also reported for PdNi.[43] The XPS analysis provides direct evidence of surface enrichment of Ni after the thermal treatment and agrees well with the composition change resulting from the outward movements of dislocation observed by *in situ* ETEM.

A direct consequence of redistribution of metal elements in a bimetallic nanoparticle catalyst is the change of its catalytic activity. Under the harsh acidic condition for ORR, activated surface of Pt-Ni or other Pt-based bimetallic catalyst typically consists of a Pt skin and Ni or other metal subsurface layer.[30] The carbon-supported Pt-Ni octahedral nanoparticle catalyst transformed the top 1.5-nm Pt-rich shell with more Ni contents on thermal treatment (Scheme 1). The CV shows flat curves for the hydrogen adsorption/desorption regions, indicating Pt(111) facet-dominant surfaces. Interestingly, the OH adsorption and desorption peaks between 0.6 and 0.8 V (vs. RHE) decreased continuously during the initial five CV cycles (Figure 6). The disappearance of these OH related peaks can be attributed to the dissolution of non-Pt metal from the surface, which was observed previously in other bimetallic electrocatalysts (Pt-Co and Pt-Cu).[32,33] After 20 CV cycles, most of Ni atoms on the outmost surface of the treated catalysts were dissolved into the acidic electrolyte, resulting in the formation of Pt skin.

These octahedral catalysts with Pt skin were then used as catalyst for ORR. A huge positive shift of 58 mV was observed in the ORR polarization measurement after the first two cycles (Figure 7). The ORR polarization shifted by another 28 mV in the same direction in the subsequent cycles before the curve was finally stabilized. The initial big jump of 58 mV could be attributed to the optimization of surface structure by removing additional Ni atoms, most likely in the top surface region. The gradual shift during the subsequent ORR polarization cycles was from the leaching of Ni atoms from the more inner and subsurface regions. Besides the applied potential, strong affinity between Ni and O atoms should also contribute to this process.[31,33] The surface structure, composing of Pt skin on Ni-containing subsurface, further optimized the reaction of oxygen with surface Pt atoms by shifting the binding energy more negatively than Pt_3Ni, namely, toward the value corresponding to the maximum current density of volcano plot. The kinetic current density (i_s) at 0.9 V had a

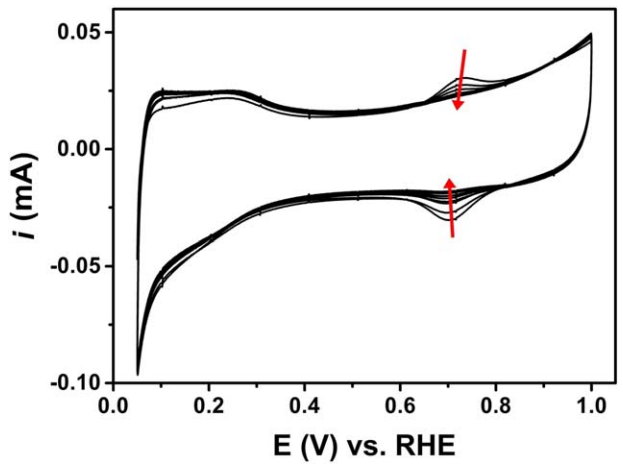

Figure 6. Initial CV scans of thermally treated Pt-Ni/C octahedral catalysts.

The CV was performed in 0.1-M $HClO_4$ under Ar. Dissociation of surface Ni was evident judging by the disappearance of peaks between 0.6 and 0.8 V (vs. RHE). [Color figure can be viewed in the online issue, which is available at wileyonlinelibrary.com.]

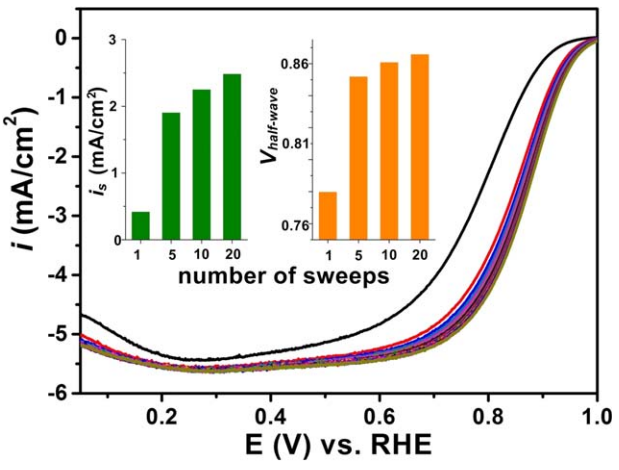

Figure 7. ORR polarization curves of thermally treated Pt-Ni octahedral catalyst after CV treatments.

Insets show the area specific and mass activity values after the designated number of cycles. [Color figure can be viewed in the online issue, which is available at wileyonlinelibrary.com.]

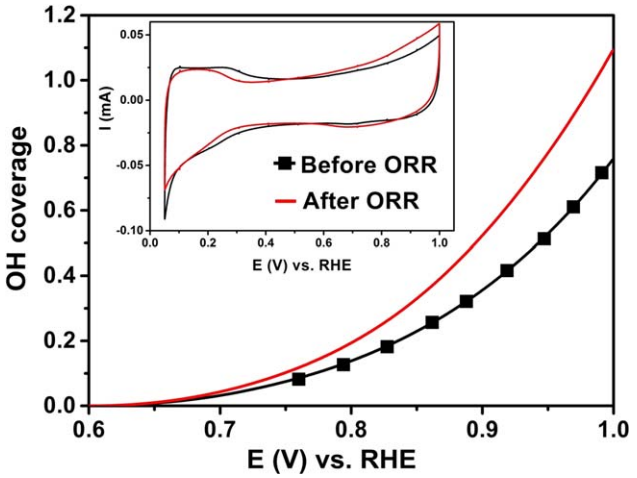

Figure 8. Coverage of hydroxyl group on surface of the Pt-Ni octahedral catalyst before and after ORR tests.

Inset shows the corresponding CV curves. [Color figure can be viewed in the online issue, which is available at wileyonlinelibrary.com.]

six-time increase, changing from 0.42 to 2.49 mA/cm^2, and the half-wave potential ($V_{\text{half-wave}}$) increased from 0.78 V for the initial to 0.866 V for the final ORR sweeps (Figure 7 inset). The catalyst had a final specific surface activity of 4.8 mA/cm$^2_{\text{Pt}}$ and mass activity of 1.4 A/mg$_{\text{Pt}}$. On the contrary, the as-made Pt-Ni sandwich catalysts had an ORR surface specific activity of 1.2 mA/cm$^2_{\text{Pt}}$ with little change over CV and ORR cycles (Supporting Information Figure S6).

A careful examination of CV curves shows the hydrogen adsorption/desorption region became narrower after cycling (Figure 8, inset). This change could be due to the oxygen-induced enrichment of Ni at surface and subsurface layer, which also altered the OH adsorption (Figure 8). Theoretical studies suggest that the adsorption strength of oxygen on the (111) surface of Pt-Ni with a Pt skin layer is slightly weaker than the required for maximum ORR activity.[44] Our study suggests that the formation of Ni-enriched near surface alloy layer changed the adsorption strength of oxygen in comparison to a pure Ni subsurface layer, because Ni in Pt causes the upshift of the d-band center of the {111} surface of Pt-Ni toward the value expected for maximum ORR activity.[44,45] Based on the above TEM, XRD, XPS observations and ORR characterization, a composition-redistribution process can thus be derived and is summarized in Scheme 1.

Conclusion

In sum, *in situ* ETEM study under reacting conditions, together with XPS data, provide direct evidence to show dislocation movement is one structural factor likely to be the origin for much enhanced ORR catalytic performance. The three-layered structure of Pt-Ni octahedral nanoparticle catalyst that has Pt-rich shell and core is rather unique and worthwhile for further exploration. The degree of enhancement in ORR activity (1.4 A/mg$_{\text{Pt}}$ in mass activity and 4.8 mA/cm$^2_{\text{Pt}}$ in area specific activity) is very high. This study highlights the tremendous potentials of postsynthesis treatment and usefulness of *in situ* ETEM in understanding the structural origins, and subsequently the design principle of optimal electronic and surface geometric configurations for catalyst.

Acknowledgments

This research is supported in part by NSF grant (Grant No.: CHE-1213926). Use of the Center for Nanoscale Materials, Frederick Seitz Materials Research Laboratory is supported by the U.S. Department of Energy, Office of Science (Contract No.: DE-AC02-06CH11357). The environmental TEM was acquired through a grant support from NSF (Grant No.: MRI-1229454) and initially set up by Professor Jian-Min Zuo. YTP is grateful for the fellowship supports from the Ministry of Education of Taiwan and Dow Chemical Company. JBW is a Shen Fellowship recipient from Department of Chemical and Biomolecular Engineering at University of Illinois.

Literature Cited

1. Wu J, Yang H. Platinum-based oxygen reduction electrocatalysts. *Acc Chem Res*. 2013;46:1848–1857.
2. Hummelshøj JS, Blomqvist J, Datta S, Vegge T, Rossmeisl J, Thygesen KS, Luntz AC, Jacobsen KW, Nørskov JK. Communications: elementary oxygen electrode reactions in the aprotic Li-air battery. *J Chem Phys*. 2010;132:071101.
3. Jung H-G, Hassoun J, Park J-B, Sun Y-K, Scrosati B. An improved high-performance lithium–air battery. *Nat Chem*. 2012;4:579–585.
4. Kim TW, Choi K-S. Nanoporous $BiVO_4$ photoanodes with dual-layer oxygen evolution catalysts for solar water splitting. *Science*. 2014;343:990–994.
5. Alayoglu S, Nilekar AU, Mavrikakis M, Eichhorn B. Ru-Pt core-shell nanoparticles for preferential oxidation of carbon monoxide in hydrogen. *Nat Mater*. 2008;7:333–338.
6. Wu J, Li P, Pan Y-T, Warren S, Yin X, Yang H. Surface lattice-engineered bimetallic nanoparticles and their catalytic properties. *Chem Soc Rev*. 2012;41:8066–8074.
7. Huang X, Zhao Z, Cao L, Chen Y, Zhu E, Lin Z, Li M, Yan A, Zettl A, Wang YM, Duan X, Mueller T, Huang Y. High-performance transition metal–doped Pt_3Ni octahedra for oxygen reduction reaction. *Science*. 2015;348:1230–1234.
8. Wu J, Gross A, Yang H. Shape and composition-controlled platinum alloy nanocrystals using carbon monoxide as reducing agent. *Nano Lett*. 2011;11:798–802.
9. Xia Y, Xiong Y, Lim B, Skrabalak SE. Shape-controlled synthesis of metal nanocrystals: simple chemistry meets complex physics? *Angew Chem Int Ed*. 2009;48:60–103.
10. Carpenter MK, Moylan TE, Kukreja RS, Atwan MH, Tessema MM. Solvothermal synthesis of platinum alloy nanoparticles for oxygen reduction electrocatalysis. *J Am Chem Soc*. 2012;134:8535–8542.
11. Vitos L, Ruban AV, Skriver HL, Kollár J. The surface energy of metals. *Surf Sci*. 1998;411:186–202.
12. Tao F, Grass ME, Zhang Y, Butcher DR, Renzas JR, Liu Z, Chung JY, Mun BS, Salmeron M, Somorjai GA. Reaction-driven restructuring of Rh-Pd and Pt-Pd core-shell nanoparticles. *Science*. 2008;322:932–934.
13. Beaumont SK, Alayoglu S, Pushkarev VV, Liu Z, Kruse N, Somorjai GA. Exploring surface science and restructuring in reactive atmospheres of colloidally prepared bimetallic CuNi and CuCo nanoparticles on SiO_2 in situ using ambient pressure X-ray photoelectron spectroscopy. *Faraday Discuss*. 2013;162:31–44.
14. Mayrhofer KJJ, Juhart V, Hartl K, Hanzlik M, Arenz M. Adsorbate-induced surface segregation for core–shell nanocatalysts. *Angew Chem Int Ed*. 2009;48:3529–3531.
15. Tenney SA, Ratliff JS, Roberts CC, He W, Ammal SC, Heyden A, Chen DA. Adsorbate-induced changes in the surface composition of bimetallic clusters: Pt−Au on TiO_2(110). *J Phys Chem C*. 2010;114:21652–21663.
16. Tao F, Salmeron M. In situ studies of chemistry and structure of materials in reactive environments. *Science*. 2011;331:171–174.
17. Zheng F, Alayoglu S, Pushkarev VV, Beaumont SK, Specht C, Aksoy F, Liu Z, Guo J, Somorjai GA. In situ study of oxidation states and structure of 4 nm CoPt bimetallic nanoparticles during CO oxidation using X-ray spectroscopies in comparison with reaction turnover frequency. *Catal Today*. 2012;182:54–59.
18. Cui C, Ahmadi M, Behafarid F, Gan L, Neumann M, Heggen M, Cuenya BR, Strasser P. Shape-selected bimetallic nanoparticle electrocatalysts: evolution of their atomic-scale structure, chemical composition, and electrochemical reactivity under various chemical environments. *Faraday Discuss*. 2013;162:91–112.

19. Chenna S, Crozier P. In situ environmental TEM studies to understand the effect of Ru promotion on supported Ni catalysts. *Microsc Microanal*. 2011;17:1602–1603.
20. Chenna S, Crozier PA. In situ environmental transmission electron microscopy to determine transformation pathways in supported Ni nanoparticles. *Micron*. 2012;43:1188–1194.
21. Chenna S, Crozier PA. Operando transmission electron microscopy: a technique for detection of catalysis using electron energy-loss spectroscopy in the transmission electron microscope. *ACS Catal*. 2012;2:2395–2402.
22. Yoshida H, Kuwauchi Y, Jinschek JR, Sun K, Tanaka S, Kohyama M, Shimada S, Haruta M, Takeda S. Visualizing gas molecules interacting with supported nanoparticulate catalysts at reaction conditions. *Science*. 2012;335:317–319.
23. Xin HL, Alayoglu S, Tao R, Genc A, Wang C-M, Kovarik L, Stach EA, Wang L-W, Salmeron M, Somorjai GA, Zheng H. Revealing the atomic restructuring of Pt–Co nanoparticles. *Nano Lett*. 2014;14:3203–3207.
24. Strasser P. Catalysts by platonic design. *Science*. 2015;349:379–380.
25. Peng Z, Yang H. Designer platinum nanoparticles: control of shape, composition in alloy, nanostructure and electrocatalytic property. *Nano Today*. 2009;4:143–164.
26. Wu J, Qi L, You H, Gross A, Li J, Yang H. Icosahedral platinum alloy nanocrystals with enhanced electrocatalytic activities. *J Am Chem Soc*. 2012;134:11880–11883.
27. Wu J, Zhang J, Peng Z, Yang S, Wagner FT, Yang H. Truncated octahedral Pt_3Ni oxygen reduction reaction electrocatalysts. *J Am Chem Soc*. 2010;132:4984–4985.
28. Zhang J, Yang H, Fang J, Zou S. Synthesis and oxygen reduction activity of shape-controlled Pt_3Ni nanopolyhedra. *Nano Lett*. 2010;10:638–644.
29. Choi S-I, Xie S, Shao M, Odell JH, Lu N, Peng H-C, Protsailo L, Guerrero S, Park J, Xia X, Wang J, Kim MJ, Xia Y. Synthesis and characterization of 9 nm Pt–Ni octahedra with a record high activity of 3.3 A/mg_{pt} for the oxygen reduction reaction. *Nano Lett*. 2013;13:3420–3425.
30. Stamenkovic VR, Fowler B, Mun BS, Wang GF, Ross PN, Lucas CA, Markovic NM. Improved oxygen reduction activity on $Pt_3Ni(111)$ via increased surface site availability. *Science*. 2007;315:493–497.
31. Ma Y, Balbuena PB. Pt surface segregation in bimetallic Pt_3M alloys: a density functional theory study. *Surf Sci*. 2008;602:107–113.
32. Cui C, Gan L, Heggen M, Rudi S, Strasser P. Compositional segregation in shaped Pt alloy nanoparticles and their structural behaviour during electrocatalysis. *Nat Mater*. 2013;12:765–771.
33. Callejas-Tovar R, Balbuena PB. Oxygen adsorption and surface segregation in (211) surfaces of Pt(shell)/M(core) and Pt_3M (M = Co, Ir) alloys. *Surf Sci*. 2008;602:3531–3539.
34. Strasser P, Koh S, Anniyev T, Greeley J, More K, Yu C, Liu Z, Kaya S, Nordlund D, Ogasawara H, Toney MF, Nilsson A. Lattice-strain control of the activity in dealloyed core–shell fuel cell catalysts. *Nat Chem*. 2010;2:454–460.
35. Kim J, Lee Y, Sun S. Structurally ordered FePt nanoparticles and their enhanced catalysis for oxygen reduction reaction. *J Am Chem Soc*. 2010;132:4996–4997.
36. Chen C, Kang Y, Huo Z, Zhu Z, Huang W, Xin HL, Snyder JD, Li D, Herron JA, Mavrikakis M, Chi M, More KL, Li Y, Markovic NM, Somorjai GA, Yang P, Stamenkovic VR. Highly crystalline multimetallic nanoframes with three-dimensional electrocatalytic surfaces. *Science*. 2014;343:1339–1343.
37. Gan L, Cui C, Heggen M, Dionigi F, Rudi S, Strasser P. Element-specific anisotropic growth of shaped platinum alloy nanocrystals. *Science*. 2014;346:1502–1506.
38. Zhang L, Roling LT, Wang X, Vara M, Chi M, Liu J, Choi S-I, Park J, Herron JA, Xie Z, Mavrikakis M, Xia Y. Platinum-based nanocages with subnanometer-thick walls and well-defined, controllable facets. *Science*. 2015;349:412–416.
39. Markus S, Michael L, Manuel R, Bogdan S. Studies of atomic diffusion in Ni–Pt solid solution by X-ray photon correlation spectroscopy. *J Phys Condens Matter*. 2013;25:065401.
40. Leitner M, Sepiol B, Stadler L-M, Pfau B, Vogl G. Atomic diffusion studied with coherent X-rays. *Nat Mater*. 2009;8:717–720.
41. Gong W, Zhang L, Yao D, Zhou C. Diffusivities and atomic mobilities in fcc Ni–Pt alloys. *Scr Mater*. 2009;61:100–103.
42. Herzig C, Divinski SV. Grain boundary diffusion in metals: recent developments. *Mater Trans*. 2003;44:14–27.
43. Shen SY, Zhao TS, Xu JB, Li YS. Synthesis of PdNi catalysts for the oxidation of ethanol in alkaline direct ethanol fuel cells. *J Power Sources*. 2010;195:1001–1006.
44. Stamenkovic V, Mun BS, Mayrhofer KJJ, Ross PN, Markovic NM, Rossmeisl J, Greeley J, Nørskov JK. Changing the activity of electrocatalysts for oxygen reduction by tuning the surface electronic structure. *Angew Chem Int Ed*. 2006;45:2897–2901.
45. Hammer B, Nørskov JK. Theoretical surface science and catalysis—calculations and concepts. *Adv Catal*. 2000;45:71–129.

Manuscript received Aug. 10, 2015, and revision received Oct. 2, 2015.